Soft Matter

Coiling of semiflexible paramagnetic colloidal chains

Journal:	*Soft Matter*
Manuscript ID	SM-ART-01-2023-000066.R1
Article Type:	Paper
Date Submitted by the Author:	02-Mar-2023
Complete List of Authors:	Spatafora-Salazar, Aldo; Rice University, Chemical & Biomolecular Engineering Kuei, Steve; Rice University, Chemical and Biomolecular Engineering Cunha, Lucas ; Rice University Biswal, Sibani; Rice University, Chemical and Biomolecular Engineering

Soft Matter

ARTICLE TYPE

Cite this: DOI: 00.0000/xxxxxxxxxx

Coiling of semiflexible paramagnetic colloidal chains

Aldo Spatafora-Salazar,[a‡] Steve Kuei,[a‡] Lucas H. P. Cunha,[a] and Sibani Lisa Biswal[a]

Received Date
Accepted Date

DOI: 00.0000/xxxxxxxxxx

Semiflexible filaments deform into a variety of configurations that dictate different phenomena manifesting at low-Reynolds number. Harnessing the elasticity of these filaments to perform transport-related processes at the microfluidic scale requires structures that can be directly manipulated to attain controllable geometric features during their deformation. The configuration of semiflexible chains assembled from paramagnetic colloids can be readily controlled upon the application of external time-varying magnetic fields. In circularly rotating magnetic fields, these chains undergo coiling dynamics in which their ends close into loops that wrap inward, analogous to the curling of long nylon filaments under shear. The coiling is promising for the precise loading and targeted transport of small materials, however effective implementation requires an understanding of the role that field parameters and chain properties play on the coiling features. Here, we investigate the formation of coils in semiflexible paramagnetic chains using numerical simulations. We demonstrate that the size and shape of the initial coils are governed by the Mason and elastoviscous numbers, related to the field parameters and the chain bending stiffness. The size of the initial coil follows a nonmonotonic behavior with Mason number from which two regions are identified: 1) an elasticity-dependent nonlinear regime in which the coil size decreases with increasing field strength and for which loop shape tends to be circular, and 2) an elasticity-independent linear regime where the size increases with field strength and the shape become more elliptical. From the time scales associated to these regimes, we identify distinct coiling mechanisms for each case that relate the coiling dynamics to two other configurational dynamics of paramagnetic chains: wagging and folding behaviors.

1 Introduction

The conformations of semiflexible filaments play essential roles in a wide variety of phenomena, ranging from biological physics to processing of polymer solutions and fiber suspensions.[1–5] In the instance of fluid flow-driven deformation, particularly that of shear flow, the competition between viscous stresses and filament elasticity leads to multiple types of morphological dynamics including buckling while tumbling,[6] snaking turns,[7] and even coiling of the ends via curling that leads to self-entanglement.[8–11] Such flow-induced microdynamics in semi-flexible filaments have been investigated extensively as they give rise to bulk rheological properties and flow behaviors,[1,12] from elastic instabilities[13–15] to shear thinning and normal stress differences.[16] Additionally, controlled manipulation of the geometric features of the deformed filaments is desirable to perform mechanical tasks at the micro-scale and enhance transport.[17–20]

Achieving precise control requires the specific design of filaments that can reconfigure in response to changes in an external field that is not imposed by the surrounding fluid.[21,22] Uniform time-varying magnetic fields satisfy this necessity. Model magnetic filaments can be produced from the directed assembly of paramagnetic colloidal particles,[23,24] which magnetize under a static magnetic field and assemble into linear chains to minimize the dipolar interaction energy between the induced magnetic moments. The induced dipoles respond quickly to changes in the direction of the magnetic field, leading to the reorientation of the chains and facilitating their manipulation with time-varying magnetic fields.[25–27] Incorporating macromolecular linkers, like DNA or adsorbing polymers, during the assembly confers elastic properties to the chains similar to conventional semi-flexible filaments.[25,28–30] Under different types of time-varying magnetic fields, these chains acquire unique morphologies like helices[31,32] and wave-like patterns.[33,34] Leveraging the dynamics of these driven colloidal systems is crucial for the propulsion of microrobots,[32,35] the pumping of particulates in microfluidic devices by mimicking ciliary strokes,[21,36–38] as well as the loading and transportation of cargo to targeted sites.[39,40]

The most common approach to actuate semi-flexible paramagnetic chains is to use an in-plane circularly rotating magnetic field (CRMF),[25,41,42] which changes direction while maintaining

Department of Chemical and Biomolecular Engineering, Rice Univeresity, Houston TX 77005

‡ These authors contributed equally to this work

a constant magnitude. The parameters of the CRMF define the interplay between viscous and magnetic stresses acting on the chains.[43,44] As a result, unique bending deformations transpire as an initially straight chain attempts to rotate and realign with the direction of the field. For instance, the ends of the chain can repeatedly deflect and straighten in a behavior denominated wagging that is analogous to a rocking motion of the tips.[45,46] In another case, both deflecting ends bend considerably by turning around and aligning parallel to the main chain backbone, folding into a clip-like configuration.[25,45]

A third type of deformation dynamics displayed under CRMF is characterized by deflecting ends that curl anti-symmetrically until the tips touch the chain backbone, forming closed loops on each side.[45,47] These coils then continue to wrap inward by progressively incorporating more segments of the central backbone into two spirals. Eventually, the entire chain collapses into an effectively smaller lasso-structure that rotates synchronously with the CRMF.[48] Similar wrapping behavior has also been reported for paramagnetic chains in the absence of macromolecular linkers, where the CRMF induces the formation of triangular clusters at both ends that then grow by rotating and consuming the backbone of the chain until both ends merge into a 2D cluster with crystalline arrangement of the colloids.[49–51] These magnetically induced coiling dynamics are also reminiscent of the self-entanglement of long filaments when subjected to very high shear rates, which start by curling ends that wrap several times to form tight loops.[8,10,11]

Recently, the coiling of semi-flexible chains was demonstrated to be viable for cargo-loading applications by enclosing non-magnetic cargo within the loops of the chain for subsequent translocation of the material by changing the type of magnetic field.[40] Thus, it is important to understand how the parameters of the CRMF and the elastic properties of a chain affect the coiling deformation process. Previous studies analyzed the propagation velocity of the coiling spirals as a function of the field strength and identified scaling laws that change according to the absence or presence of elastic linkers.[47,49]

In this work, we employ numerical simulations to characterize the morphology and size of the first loop formed during the anti-symmetric coiling process of bead-spring paramagnetic chains of different stiffness deformed under various CRMF parameters. Furthermore, we find relevant time-scales for the formation of the first loop, and identify two regimes based on the size of the initial loop, each having distinct shapes, time-scales, and mechanisms of deformation. These regimes indicate that the wagging and folding behaviors of semi-flexible chains are limits of the coiling dynamics under certain conditions of the field strength. Our results demonstrate how the CRMF parameters control the geometric characteristics of the loops by changing the mechanism of coiling deformation.

2 Theoretical Modeling

We employ a similar theoretical framework as our previous work on the sedimentation of elastic filaments[52] and the actuation of colloidal chains in complex time-varying fields,[34] where the simulation technique is based on a deterministic overdamped equation of motion with hydrodynamic interactions between particles. The colloidal chains are modeled as a bead-spring system confined in 2D and consisting of $N = 101$ spheres of radius a with their centers connected by $N-1$ mass-less springs of length $l_0 = 5a/2$. Naturally, the spheres and springs represent the paramagnetic colloids and linkers like DNA, respectively, from experimental systems. Hence, the contour length of the chains is $L = 5a(N-1)/2$. The suspending medium is assumed to be a Newtonian fluid of viscosity η. Since the chain sizes are microscopic and the coiling events arise at velocities in the order of the field frequency or slower, inertial effects are neglected, leading us to the Stokes regime. Non-local hydrodynamic interactions were only accounted for between the beads, neglecting the presence of the springs and nearby walls. Therefore, the velocities of the particles are formulated as a linear function of the non-hydrodynamic forces acting on them and their relative spatial arrangement via the mobility formulation

$$\mathbf{v}_{\mathrm{i}} = \sum_{\mathrm{j}=1}^{N} \mathbb{G}^{\mathrm{ij}} \cdot \mathbf{F}_{\mathrm{j}}^{\mathrm{nh}} \quad \text{for i, j} = 1,\ldots,N; \tag{1}$$

where $\mathbf{v}_i$ is the velocity of the ith particle, $\mathbf{F}_{\mathrm{j}}^{\mathrm{nh}}$ is the sum of the nonhydrodynamic forces acting on the jth bead, and $\mathbb{G}^{\mathrm{ij}}$ is a 3×3 mobility tensor encoding the separation between the ith and jth particles that describes the hydrodynamic interactions mediated by the fluid and correlates the dynamics of the two particles. In this work, we use the Rotne-Prager-Yamakawa mobility tensor given by[53,54]

$$\mathbb{G}^{\mathrm{ii}} = \frac{\mathbf{I}}{6\pi\eta a} \tag{2a}$$

$$\mathbb{G}^{\mathrm{ij}} = \frac{1}{8\pi\eta}\left\{\frac{1}{r}[\mathbf{I}+\hat{\mathbf{r}}\hat{\mathbf{r}}] + \frac{2a^2}{3r^3}[\mathbf{I}-3\hat{\mathbf{r}}\hat{\mathbf{r}}]\right\} \text{ for i} \neq \text{j}, \tag{2b}$$

where $\mathbf{I}$ is the identity tensor, $\mathbf{r}$ is the distance vector between the particle pair, $r = \|\mathbf{r}\|$ is its magnitude, and $\hat{\mathbf{r}} = \mathbf{r}/r$ is its direction. Note that Brownian fluctuations are not considered in this formulation since we are interested in understanding the deterministic dynamics of the system.

Having formulated the mobility problem, the next step is to compute the nonhydrodynamic forces acting on each bead. Here, the forces of interest are elastic and magnetic. The elastic terms consist of stretching and bending forces that arise from the springs connecting adjacent particles, which in the experimental system define the rigidity and extensibility of the chains. We define the local energies of stretching and bending as

$$U^s = \frac{\sigma_s}{2l_0}(r-l_0)^2 \text{ and } U^b = \frac{\sigma_b}{2l_0}(\theta-\theta_0)^2 \tag{3}$$

where σ_s and σ_b are the stretching and bending moduli, respectively, θ is the angle formed between two adjacent segments connecting three neighboring beads, and θ_0 is the equilibrium angle between the segments. Assuming that the chain can be modeled as an elastic filament with a circular cross-section of radius equal to the particle radius a, we set the relationship between the moduli to be $\sigma_s = 4\sigma_b/a^2$ based on Euler-Bernoulli beam theory. Additionally, we impose $\theta_0 = 0$ in order to study chains of zero intrinsic curvature, *i.e.* the chains have a linear shape when unperturbed.

The elastic forces are then computed as

$$\mathbf{f}^s = -\nabla U^s \text{ and } \mathbf{f}^b = -\nabla U^b. \tag{4}$$

The magnetic forces on the beads arise from the interaction between the particles' magnetic dipoles, which are induced by the spatially uniform external magnetic field. To account for these dipole-dipole interactions in the simulations, we employ the mutual dipolar model (MDM),[55,56] in which the magnetization $\mathbf{m}$ of one bead depends on the intensity of the external field $\mathbf{H}_0$ and the magnetization of the other particles along the chain

$$\mathbf{m}_\mathrm{i} = \frac{4}{3}\pi a^3 \chi \left[\mathbf{H}_0 + \sum_{\mathrm{j}\neq\mathrm{i}}^{N} \mathbb{M}^{\mathrm{ij}} \cdot \mathbf{m}_\mathrm{j}\right] \tag{5}$$

where χ is the effective magnetic susceptibility of the particles, and $\mathbb{M}^{\mathrm{ij}} = (3\mathbf{rr}/r^5 - \mathbf{I}/r^3)/4\pi$ is the grand potential tensor that describes the mutual induction effect between the dipoles of different particles.[57] The external circularly rotating magnetic field (CRMF) is spatially uniform and rotates in the plane of the chains, as defined by

$$\mathbf{H}_0(t) = H_0\{\cos(2\pi f t)\hat{\mathbf{e}}_x + \sin(2\pi f t)\hat{\mathbf{e}}_y\}, \tag{6}$$

where H_0 is the field amplitude, f is the field frequency, and t is time. Note that the circularly rotating field has a time-independent magnitude that is equal to the amplitude: $\|\mathbf{H}_0\| = H_0$.

Equation 5 leads to a linear system that depends on the spatial configuration of the beads and whose solution provides the dipole moment of each one. After computing these dipole moments, the magnetic force acting on each particle is determined by[48]

$$\mathbf{f}_\mathrm{i}^{\mathrm{mag}} = -\sum_{\mathrm{j}\neq\mathrm{i}}^{N} \frac{3\mu_0}{4\pi r^5}\left[(\mathbf{m}_\mathrm{i}\cdot\mathbf{r})\mathbf{m}_\mathrm{j} + (\mathbf{m}_\mathrm{j}\cdot\mathbf{r})\mathbf{m}_\mathrm{i} + (\mathbf{m}_\mathrm{i}\cdot\mathbf{m}_\mathrm{j})\mathbf{r} - 5\frac{(\mathbf{m}_\mathrm{i}\cdot\mathbf{r})(\mathbf{m}_\mathrm{j}\cdot\mathbf{r})\mathbf{r}}{r^2}\right] \tag{7}$$

where μ_0 is the magnetic permeability of the vacuum.

The last nonhydrodynamic force to consider arises from steric interactions that prevent spatial overlap between particles that come into contact. Here, we employed the Hertz force description[58,59] with an empirically chosen elastic modulus of the beads to account for the steric effects.

Upon computing the nonhydrodynamic forces and calculating the particle velocities $\mathbf{v}_\mathrm{i}$ from Eq. 1, the particle positions are evolved in time by

$$\mathbf{x}_\mathrm{i}(t+\Delta t) = \mathbf{x}_\mathrm{i}(t) + \Delta t \mathbf{v}_\mathrm{i}(t) \tag{8}$$

where Δt is the time-step.

The problem was nondimensionalized using the chain contour length L for distance, the field frequency f for time, H_0 for the magnetic field strength, and $4\pi a^3 \chi H_0$ for the magnetization of the beads. The equations of motion in our model are defined by two dimensionless groups. The first is the Mason number, Ma, which describes the ratio of viscous to magnetic forces[60,61]

$$\mathrm{Ma} = \frac{144\pi\eta f}{\mu_0 \chi^2 H_0^2}. \tag{9}$$

The second is the Magnetoelastic number, Mn, that defines the ratio of magnetic to bending stresses[33]

$$\mathrm{Mn} = \frac{\pi a^2 \mu_o H_o^2 L^2}{6\sigma_b} \frac{\chi^2}{(1-\chi/6)(1+\chi/12)}. \tag{10}$$

Ma compares the effects of the two field parameters (H_0 and f), while Mn expresses how the strength of the external magnetic field can overcome the flexural rigidity of the chain. However, to probe for the effective stiffness of the chain, the dimensionless numbers must account for the ratio between viscous and bending forces. Therefore, we introduce the elastoviscous number, A, as a third dimensionless group that defines this ratio based on the product of Ma and Mn

$$A = \frac{\mathrm{MaMn}}{N^2}\left(1-\frac{\chi}{6}\right)\left(1+\frac{\chi}{12}\right) = \frac{24\pi^2 a^2 L^2 \eta f}{\sigma_b N^2}. \tag{11}$$

Note that A is analogous to the dimensionless term employed to analyze the morphological dynamics of semiflexible polymers in shear flow that compares strain rate to the bending modulus of the fibers.[5,7,10] In this work, we probe the coiling dynamics for various effective stiffness A while varying Ma. As Ma is increased, Mn is decreased accordingly to maintain a constant A, which would be analogous to performing experiments at constant frequency f on chains with the same σ_b while testing different field strengths H_0.

3 Results and Discussions

In our previous work,[45,48] the different dynamics undergone by DNA-linked paramagnetic colloidal chains were mapped on a state diagram according to the Mason number, Ma (Eq. 9), and the number of particles in the bead-chain, N. The four types of dynamics identified were synchronous rotation, wagging, folding, and coiling. The latter three are characterized by distinct types of deformation. Long chains display these three configurational dynamics based on Ma, which is defined by the CRMF parameters. Folding and wagging deformations manifest at low and high Ma, respectively, while the coiling dynamics appear at intermediate Ma. A schematic of this state diagram is presented in Fig. 1a, including visuals of the characteristic morphologies observed in each dynamical mode. The hatched region highlights the portion of the state diagram that is the focus of this work: the coiling of long paramagnetic chains, over a range of Ma.

The coiling of experimental chains synthesized from micron-sized superparamagnetic polystyrene particles (Dynabeads My-One Streptavidin C1, Invitrogen) linked by biotinylated DNA strands is shown in Fig. 1b-c, following a previously reported assembly method.[34,45,52,62,63] This coiling behavior occurs because the viscous forces prevent the chain from rotating synchronously with the CRMF. Instead, only the ends of the chain respond by realigning with the field direction because the particles in these regions experience less drag. The backbone of the chain remains

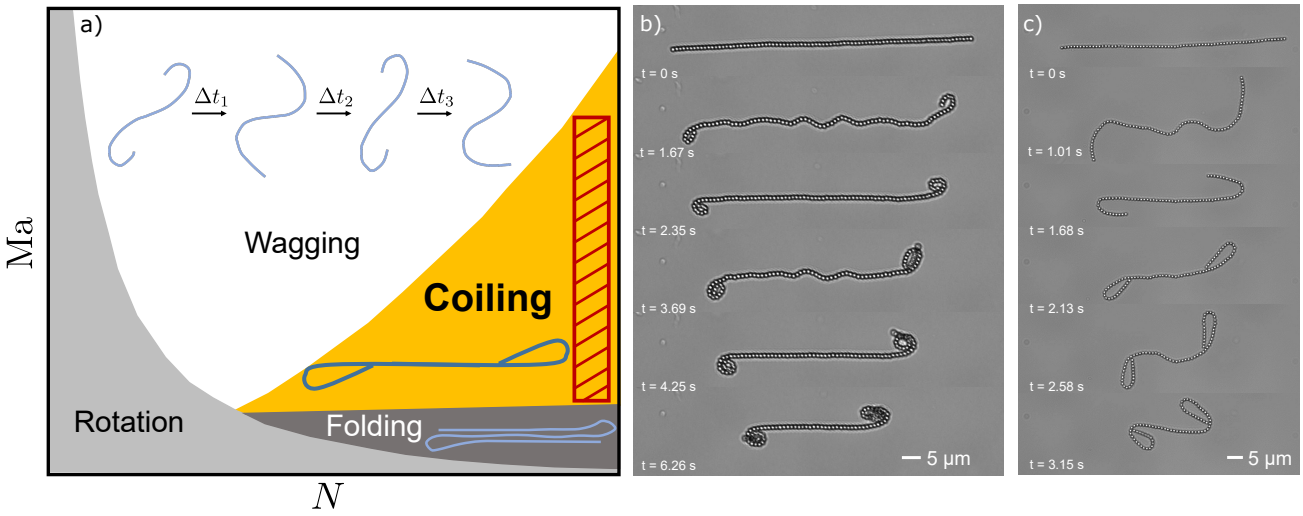

Fig. 1 Coiling dynamics of semiflexible chains composed of paramagnetic particles induced by a CRMF. a) Schematic of the state diagram of chain dynamics reported in our previous work on DNA-linked paramagnetic chains.[45,48] The chains can undergo four types of dynamics based on the Mason number (Ma) and the number of particles (N) in the chain: rigid rotation, wagging, folding, and coiling. The characteristic configurations of the three deformation dynamics are schematically represented. The hatched area indicates the region of the state diagram studied in the rest of the paper, corresponding to the coiling of long chains. b) and c) Paramagnetic chains linked by 2000 bp DNA undergoing coiling dynamics in experiments when subjected to CRMF with different parameters. b) A chain of $N = 85$ beads driven by a CRMF with strength $H_0 = 24.9$ G and frequency $f = 0.5$ Hz. c) A chain of $N = 72$ beads driven by a CRMF with $H_0 = 48.6$ G and $f = 0.3$ Hz. Chains were initialized from the straight configuration. The morphology of the coils changes with the parameters.

relatively stationary, although part of it buckles to compensate for the mismatch in orientations between different segments. Buckling instabilities occur due to repulsive dipolar interactions between the linked particles. The ends curl to align with the external field, first becoming first anti-parallel to the chain backbone, then orienting towards the backbone, and finally closing into loops.[45,47] Note that as the chain ends coil, the bending curvature propagates outward. After the first loop is formed on each side, the curling process is repeated, forming spirals around the initial loops. The chains are initialized from a straight configuration when the CRMF is applied, allowing for the coiling of both ends in an anti-symmetric fashion (S-shape). It is important to emphasize this initial condition because previous work has demonstrated asymmetric coiling (J-shape), where only one end of the chain undergoes coiling, typically when starting from bent chain configurations.[30,40]

Even though the chains in Fig. 1b and 1c both undergo anti-symmetric coiling dynamics, the shape and size of the coils can vary according to the field parameters. These differences imply that the deformed morphologies attained during the coiling process are not homogeneous inside the region of the state diagram (Fig. 1a) in which these dynamics occur. For instance, the initial loops formed in Fig. 1b are small and have a more circular shape. In contrast, the first coils formed by the ends of the chain in Fig. 1c are larger and have a more pronounced elliptical shape. Here, we characterize the initial loops as they define the rest of the coiling process. However, the experimental chain models are prone to local elastic heterogeneities along their length during the assembly process, as well as perturbations caused by Brownian motion. Coil shapes and sizes are difficult to assess for a given experimental condition, thus simulations are used to better understand the impact of magnetic field and chain elasticity on coil properties.

Time-sequences of the coiling dynamics obtained from the numerical simulations of chains with the same length, but with varying Elastoviscous number A and actuated by CRMFs of different Ma, are shown in Fig. 2. The shaded snapshots highlight the first coiling loops formed in each case. For a fixed effective stiffness A, the geometry of the first loops varies from compactly folded structures Ma (Fig. 2a) to oval shapes with progressively less curvature but with different sizes (Fig. 2b-c) as Ma increases. Recall that a higher Ma at a fixed A implies a decrease in the field strength and a simultaneous decrease in the Mn. Hence, the initial coiling loops tend to become less compact because the weaker fields cannot induce significant curvature as the chain ends are curling. These results agree with our experimental observations from Fig. 1b-c where the geometry of the coiling loops is affected by the magnitude and frequency of the magnetic field. Interestingly, the initial compact coil in Fig. 2a is reminiscent of the morphology acquired by the chains in the folding regime of Fig. 1a. However, the scenario presented in Fig. 2a differs from the conventional folding regime in two ways. First, the coil is of shorter length, and second, the chain coils several times. In the folding regime, once the chain bends into the clip-like morphology, the entire chain immediately starts to rotate synchronously with the CRMF as a rigid body. The effect of Ma on the coil size is less clear than the impact on shape. The size of the initial coils relative to the total chain length, in terms of a long-axis, appears to decrease with increasing Ma from Fig. 2a to 2b, but then increases with Ma, shown in Fig. 2c. The impact of field parameters on the size of the coil, particularly on its radius of gyration, will be discussed later here in more detail.

The stiffness of the chains also alters the geometry of the coil-

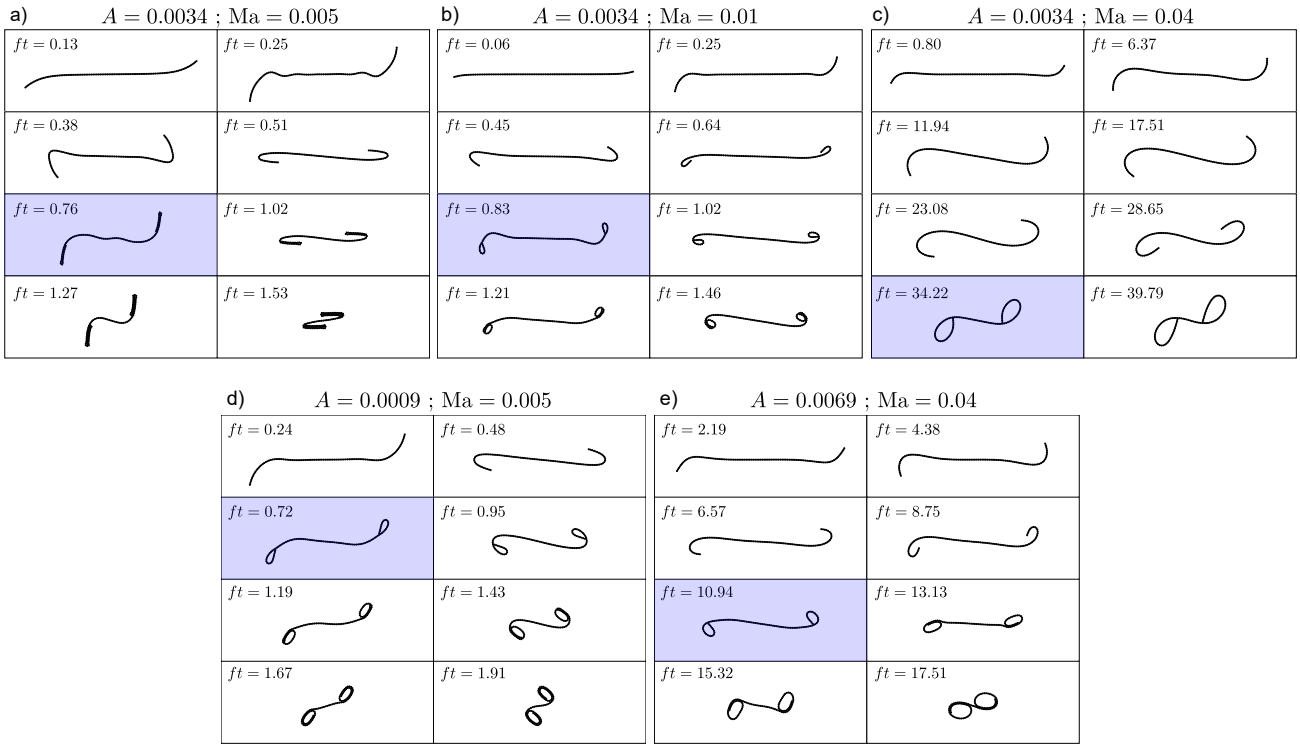

Fig. 2 Coiling dynamics obtained from numerical simulations for different cases of dimensionless parameters. Snapshots shaded in blue correspond to the first coils formed in each case and illustrate how A and Ma alter the morphology. Chains with the same effective stiffness $A = 0.0034$ undergoing coiling deformation at various CRMF conditions: a) Ma = 0.005, b) Ma = 0.01, and c) Ma = 0.04. Chains with different stiffness: d) $A = 0.0009$ at Ma = 0.005, and e) $A = 0.0069$ at Ma = 0.04. The chain in d) is stiffer than a) and under the same CRMF conditions. Likewise, the chain in e) is more flexible than the one in c). After the initial coils are formed, the chains continue to wrap along the backbone.

ing loops for a fixed Ma. This fact becomes apparent by comparing the shapes of the loops in Fig. 2a with those in 2d, where a decrease in A changes the configuration of the initial loops from folded structures (Fig. 2a) to less eccentric ellipses (Fig. 2d). This change is expected, as the lower A signifies an increased stiffness and a lower Mn. Consequently, the initial loop must have a less compact configuration because the same field strength cannot bend the stiffer chain to the same extent. It is also worth pointing out that the initial loops also became shorter after decreasing A. In contrast, decreasing the stiffness at fixed but larger Ma led to shorter loops, as seen from the comparison between Fig. 2c and 2e. This trend might be counter-intuitive at first glance. In the earlier case (Fig. 2a to 2d), the size of the initial loops decreased with decreasing A, while in this new scenario (Fig. 2c to 2e) the loops also shortened with increasing A. The only difference between these changes is the value of Ma. However, in the latter case the decrease in size was accompanied by a more compact shape of the loops, as the chain in Fig. 2e is more flexible. This qualitative analysis reveals that the relationship between the geometry of the coils and the parameters is not straightforward. A quantitative analysis is required to understand how the features of the initial loop are controlled by A and Ma.

The first loop is defined in the simulation when a bead gets in contact with a particle that is not one of its neighbors in the linear configuration. To characterize the geometric features of the first loop formed during the coiling dynamics, the gyration tensor is computed[50,64]

$$S_{nm}^{\text{loop}} = \frac{1}{2\nu^2} \sum_{\text{i}=1}^{\nu} \sum_{\text{j}=1}^{\nu} (x_n^{\text{i}} - x_n^{\text{j}})(x_m^{\text{i}} - x_m^{\text{j}}) \tag{12}$$

where ν is the number of beads that make up the loop and x_n^{i} is the n-th component of the position of the i-th particle. Note that $\nu < N/2$ because coiling occurs on both ends of the chain antisymmetrically. For two dimensions, Eq. 12 has two eigenvalues, λ_1 and λ_2, that define the principal axes of the ellipse that best fits the mass distribution of the coil. This is depicted schematically in Fig. 3. The sum of the eigenvalues yields the radius of gyration[64,65]

$$R_g^{\text{loop}} = \sqrt{\lambda_1 + \lambda_2}, \tag{13}$$

which we use to quantify the size of the initial coils. The eigenvalues of S_{nm}^{loop} are also required to compute the two-dimensional version of the asphericity parameter,[7,65]

$$\delta^{\text{loop}} = 1 - \frac{4\lambda_1\lambda_2}{(\lambda_1^2 + \lambda_2^2)^2}, \tag{14}$$

which ranges from 0 to 1 and provides a metric of the shape of the loops. As shown in Fig. 3, an asphericity equal to zero describes a circle, while a value of unity represents a straight line. Intermediate values of asphericity describe an ellipse, with increasing values representing ellipses of higher aspect ratio.

Figure 4a shows how the size of the coil changes as a function of Ma for chains of the same length and with varying A. For a fixed

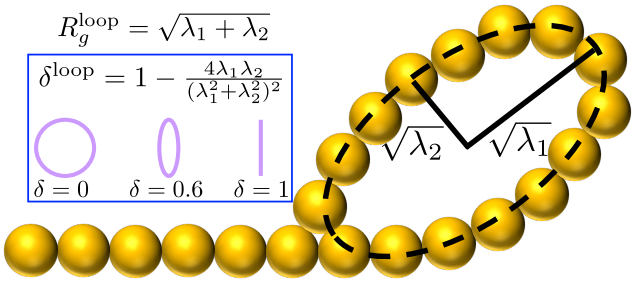

Fig. 3 Schematic of the ellipse fitting a coiling loop with principal axes corresponding to the eigenvalues (λ_1 and λ_2) of the gyration tensor. To quantify the size and shape of the loop, the radius of gyration and the asphericity are computed from the eigenvalues. The asphericity ranges from 0 to 1, where 0 defines a circle and 1 represent a straight line.

value of A, changes in Ma cannot be caused by modifying the frequency f of the CRMF or the viscosity η of the fluid because both Ma and A depend on these parameters. Instead, changes in Ma must strictly be produced by the application of a magnetic field with different strength H_0. Since $H_0 \sim \text{Ma}^{-1/2}$ (Eq. 9), we plot R_g^{loop} as a function of $\text{Ma}^{-1/2}$ to indicate that an increase in this value is equivalent to a direct increase in the magnitude of the CRMF for a chain of effective stiffness A. Note that R_g^{loop} is normalized by the chain contour length L due to the nondimensionalization of the numerical method. Interestingly, Fig. 4a demonstrates that R_g^{loop} follows a nonmonotonic trend with the field intensity. The size of the initial coiling loop shrinks as the strength of the magnetic field increases. For these conditions, the decay of R_g occurs nonlinearly as a power law. At an intermediate strength, the initial loop attains a minimum size. Afterward, the initial loop increases linearly with increasing field intensity. This nonmonotonic trend clarifies the qualitative observations from Fig. 2a-c where the initial coil got shorter after increasing Ma and then grew upon further increase in Ma.

The power of the nonlinear regime at low $\text{Ma}^{-1/2}$ depends on A. In fact, the power decay ranges from approximately -0.8 to -1.9 as A increases (see Table 1). Therefore, more flexible chains exhibit a more drastic shrinkage in their initial loop size when subjected to a smaller change in magnetic field strength than stiffer chains. In addition, the nonlinear regime is shifted to weaker fields as A increases. A decaying power-law of the radius of curvature with field intensity was previously reported by Yang *et al.*[40] for the asymmetric (one-sided) coiling of very short chains consisting of paramagnetic particles linked by entangled PVP brushes. The value of the decaying exponent in their experimental work is -2/3, so the impact of the field intensity is less drastic than the results obtained here. Additionally, this power-law was shown only for one chain stiffness. It is important to note that the radius of curvature measured for those chains corresponded to the final microlasso configuration. On the other hand, the radius of gyration computed in this study defines the size of the initial coiled configuration in long chains undergoing anti-symmetric (two-sided) coiling. Hence, exact comparisons between these results must be done with discretion. Nonetheless, the agreement in the nonlinear dependence indicates that the characteristic dimensions for both types of coiling dynamics at different stages of the wrapping process can be drastically affected by the field strength. Moreover, our results expand upon previous work by demonstrating that the power-law depends on the elastic properties of the chains. Consequently, it is possible that by assembling experimental chains of lower bending modulus, more pronounced shrinkage in loop size could be produced when applying stronger CRMFs. Having the capability to deform the chains into tighter coils could lead to greater control of cargo loading in contexts where accurate dosage is necessary, like in targeted drug delivery.

To our knowledge, the linear regime of coil size observed at higher $\text{Ma}^{-1/2}$ has not been reported previously. Surprisingly, in contrast to the power-law regime, the linear trend observed at higher $\text{Ma}^{-1/2}$ in Fig. 4a behaves independently of A. The only difference is that the linear trend is shifted to lower field intensities for larger A due to the faster decay in initial coil size experienced by more flexible chains in the nonlinear regime. This fact suggests that the elasticity of the chain does not play a significant role in defining the coil size at higher field strengths. In this regime, we find that the radius of gyration increases as

$$\frac{R_g^{\text{loop}}}{L} \sim 0.003\text{Ma}^{-1/2} \tag{15}$$

for every A, with only minor deviations in the value of each slope as shown in Table 1. To explain such a trend, we performed a torque balance between magnetic and viscous contributions acting on a mobile end of the chain. From this analysis, we obtain a theoretical prediction for R_g^{loop} as a function of $\text{Ma}^{-1/2}$ that also depends on the radius of the particles. Accounting for the particle size used in the simulations, the expression becomes

$$\frac{R_g^{\text{loop}}}{L} \approx 0.00313\text{Ma}^{-1/2}, \tag{16}$$

which has excellent agreement with the linear fits in Fig. 4a (see Table 1). This prediction strengthens the statement that the elasticity of the chain does not play a significant role in the linear regime of Fig. 4a, since the analysis yielded an expression that agrees with the simulation results despite the omission of bending moments in the torque balance. The full derivation of Eq. 16 is presented in the Appendix.

Table 1 Fitting parameters of R_g^{loop}/L for each A in the nonlinear and linear size regimes. The error of the slope is calculated with respect to the theoretically predicted slope from Eq. 16

A	Power	Slope	Slope Error (%)
0.0004	-0.77	0.00295	5.75
0.0009	-0.84	0.00291	7.03
0.0017	-1.12	0.00306	2.24
0.0034	-1.30	0.00316	0.96
0.0069	-1.90	0.00307	1.92

The linear regime represents a parameter space in which progressively longer portions at the chain ends can be actuated because the magnetic torque becomes larger as the field strength is increased. These longer segments then curl as they attempt to minimize their misalignment with the instantaneous direction of the CRMF. Since the driven segments eventually constitute the

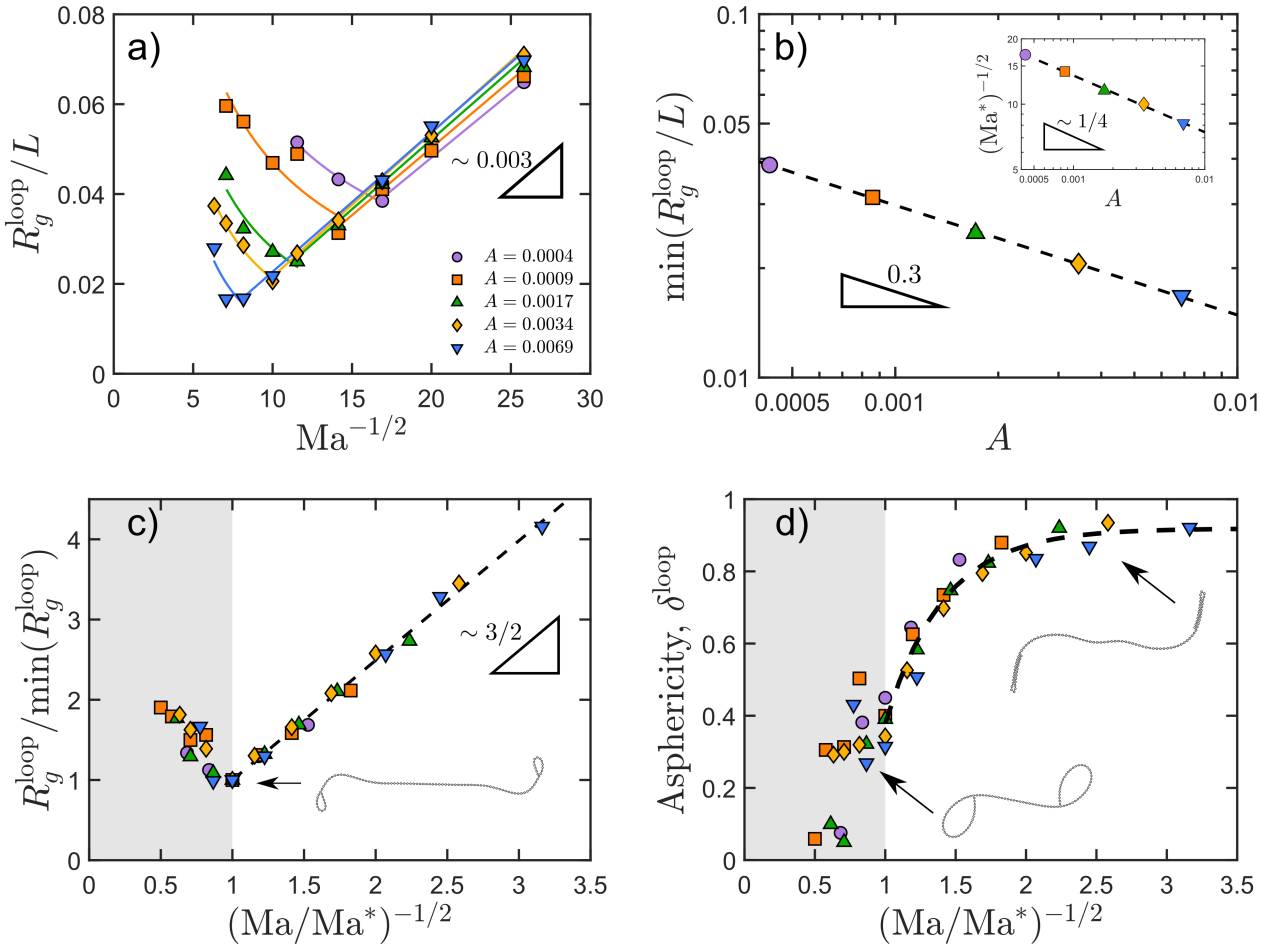

Fig. 4 Size and shape of the initial loop formed during chain coiling as a function of field parameters and chain stiffness. a) Nonmonotonic behavior of the radius of gyration of the first coil (R_g^{loop}), normalized by the chain length L, as a function of $\mathrm{Ma}^{-1/2}$ for various A. The size decreases nonlinearly with $\mathrm{Ma}^{-1/2}$ below the minimum point and increases linearly above the minimum. The linear trend has a constant slope independent of A. The minimum point shifts to weaker $\mathrm{Ma}^{-1/2}$ as A is increased. b) The minimum R_g^{loop} decreases with increasing A as a power-law with exponent of -0.3. Inset: The inverse of Ma^*, which is the Mason number at which each minimum R_g^{loop} is obtained, also decreases with A as a power-law with an exponent of approximately -0.25. c) Master curve of the loop size upon normalizing each data series by their minimum points. The shaded region indicates the nonlinear region of size. An example of a coiled chain (from Fig. 2b) at a minimum point is presented. (d) Asphericity of the first loop δ^{loop} as a function of the normalized Mason number. The shaded region indicates the non-linear size regime. Examples of coil shapes in the nonlinear and linear region are shown, corresponding to the first coils from Fig. 2a and 2c.

first loops on each side of the semi-flexible chain, then R_g^{loop} must grow accordingly with rising field strength. This regime seems to be an extension of the dynamics displayed by paramagnetic chains that do not have linkers binding the particles. Increasing the magnetic torque overcomes the viscous drag experienced by rotating unlinked chains and allows longer chains to rotate synchronously with the instantaneous direction of the CRMF without breaking up into smaller chains.[44,66–68] This increase in length can be modeled by a similar torque balance and follows a scaling of $N \sim \text{Ma}^{-1/2}$,[43,60] where N is the maximum number of particles that will undergo synchronous rotation as a single chain at a given Ma. This same scaling applies for very rigid chains that are linked by short molecules, like glutaraldehyde, for which chains longer than N particles would undergo rigid asynchronous rotational dynamics.[25] In this work, we have shown that a similar scaling is applicable to segments of semi-flexible chains actuated above a transition field strength. Furthermore, the scaling demonstrates that the size of the loop above that transition point does not depend on the stiffness of the semi-flexible chain.

The smallest coil size is attained at the transition between the nonlinear and linear regimes, shown by the minimum point for each A in Fig. 4. As shown earlier, the minimum point shifts to weaker fields as A increases. In fact, Fig. 4b shows that the decrease in the transition point follows a power scaling of $(R_g^{\text{loop}}/L)_{\text{min}} \sim A^{-0.3}$. The inset of Fig. 4b shows that Ma^*, which is the Mason number corresponding to each minimum of R_g^{loop}, also changes via a power-law scaling of $(\text{Ma}^*)^{-1/2} \sim A^{-0.25}$. Since lower stiffness allows for larger bending curvatures to develop, then loops of smaller size can be produced with weaker fields at the transition point. Upon normalizing the curves of A in Fig. 4a by their values of $(R_g^{\text{loop}})_{\text{min}}$ and $(\text{Ma}^*)^{-1/2}$ from Fig. 4b, the entirety of the data collapses into a single curve shown in Fig. 4c. The shaded region indicates the nonlinear regime in the master curve. These results highlight how to produce an initial coiling loop of a desired size under a CRMF. By knowing the bending modulus of a chain and setting the CRMF frequency, A can be calculated. Then, the value of A determines the minimum R_g^{loop} and its corresponding $(\text{Ma}^*)^{-1/2}$ by using the scalings from Fig. 4b and its inset, respectively. Finally, upon deciding the operating field strength $\text{Ma}^{-1/2}$, the minimum point values can be used to find the size of the initial loop from Fig. 4c.

The analysis of the loop sizes up until this point has not provided any insight about the different shapes they can acquire. The asphericity δ^{loop} presented in Fig. 4d as a function of the normalized Mason number shows the impact that the CRMF parameters have on the shape of the initial coil. In contrast to the size, δ^{loop} increases monotonically until it eventually reaches a plateau at high field intensities. Therefore, the initial coils tend to have a circular shape under weak fields and become more elliptical as the strength is increased. Eventually, the coil shape reaches a plateau at $\delta^{\text{loop}} = 0.93$ instead of continuing the ascent to 1. Asphericities closer to unity are not feasible because of the curvature of the loop and the excluded volume of the particles, *i.e.* the coil shape cannot collapse into a straight line. The shaded region in Fig. 4d indicates once again the nonlinear size regime from Fig. 4c. Hence, the elasticity-dependent nonlinear regime is characterized by large circular loops that progressively deviate from a circle as they shrink with rising field strength. On the other hand, the elasticity-independent linear regime forms elliptical loops that approach the limit of a straight line as they grow with increasing field strength. The values of δ^{loop} in the linear size regime increase via a saturating exponential function $\delta^{\text{loop}} = B - C\exp(-k((\text{Ma}/\text{Ma}^*)^{-1/2} - 1))$ as indicated by the dashed curve in Fig. 4d, where B, C, and k are fitting parameters. These simulation results agree the qualitative observations from the experimental colloidal chains shown in Fig. 1, where increasing the value of $\text{Ma}^{-1/2}$ from Fig. 1b to 1c yielded coiling loops that are more elliptical.

It should be emphasized that the compact folded first loop observed in Fig. 2a corresponds to high values of δ^{loop} and consequently this type of coil manifests in the linear size regime. The elliptical loops from Fig. 2b and 2d correspond to the minimum points of $A = 0.0034$ and $A = 0.0009$, respectively. Since the case in Fig. 2b is the more flexible of these two, then a weaker field (higher Ma) is capable of deforming the chain ends into smaller coils compared to Fig. 2d. Finally, the initial circular loops in the dynamics of Fig. 2c and 2e appear in the nonlinear size regime. Once more, the same field intensity can curl the ends of the more flexible chain (Fig. 2e) into smaller circular loops, compared to the stiffer chain (Fig. 2c). To better connect the loop morphologies observed in Fig. 2 with the quantitative results presented in Fig. 4, the initial loops of some of these cases are drawn inside Fig. 4c and 4d.

Having characterized the morphological features of the initial loop, we can now elucidate the mechanism of coiling deformation occurring in both size regimes. We address this part of the problem by focusing on the time-scales for initial coil formation. Figure 5a showcases the number of cycles $(ft)^{\text{loop}}$ of the CRMF required to form the first loop for each A as a function of the normalized field intensity $(\text{Ma}/\text{Ma}^*)^{-1/2}$. The normalization collapses the results into a single master curve. Once again, the shaded area indicates the nonlinear size regime. In this region, it takes less cycles to form the first loop as the magnetic field strength is increased. The decay in number of cycles approximately follows the power law scaling $(ft)^{\text{loop}} \sim [(\text{Ma}/\text{Ma}^*)^{-1/2}]^{-14/3}$. Despite the decay with field strength, it takes more than one cycle of rotation to form the coils in this nonlinear region. The only exceptions are the minimum points of the R_g^{loop} curves, which form their coil at a constant value of approximately 0.685 for every A, as seen in Fig. 5b. Furthermore, since the curves of R_g^{loop} in Fig. 4a shift to weaker field intensities as A increases, then chains that are more flexible require less cycles than their stiffer counterparts to coil at a fixed $\text{Ma}^{-1/2}$. This fact is showcased in the inset of Fig. 5a where the Mason number is not normalized by the value at the minimum point. Interestingly, $(ft)^{\text{loop}}$ decreases slightly from the minimum point and remains constant when the dynamics change to the stiffness-independent linear growth regime (Fig. 5a). This constant is $(ft)^{\text{loop}} \approx 0.6$. Hence, the initial loops form in this region in a little under 2/3rds of a period of the CRMF, regardless of the applied field strength and the size of the resulting coil.

These time scales provide insights into the mechanisms of coiling occurring in each regime. The strong fields in the linear

regime can exert a significant magnetic torque on the end segments to drive their reorientation almost synchronously from the starting straight configuration. Essentially, as the field rotates from the x-direction to the y-direction, these end segments follow the field with a small misorientation and eventually achieve a vertical orientation. During this stage of the response, bending waves travel from the chain ends to the backbone, with the inward propagation length of the bending wave increasing upon applying a stronger field intensity. Once the magnetic field direction rotates toward the negative x-direction, the curvature begins to propagate outward to accommodate for the curling of the vertical end segments that continue to rotate synchronously with the field. Hence, the chain ends becoming anti-parallel to the chain backbone around half a period of the magnetic field. The inward and outward propagation of the curvature can be seen from the simulation snapshots occurring prior to the blue-shaded panels of Fig. 2a, 2b, and 2d. Afterward, as the field rotates toward the negative y-direction, the anti-parallel ends continue to follow the field direction until the tips touch the chain backbone and form the coiling loop. Consequently, the chain attains its initial coiled state before the magnetic field has completed a single revolution. This process is independent of the elastic properties of the semiflexible chain and increasing the field strength leads to a longer portion of the chains to deflect, leading to a larger loop size.

Since the coiling loops formed at large field strengths have a compact folded shape and require less than a single cycle to form, like those attained in Fig. 2a, we can connect the coiling dynamics to the folding configurations presented in the schematic of Fig. 1a. Further increasing the field strength in the linear regime of coiling size will eventually increase the length of the mobile end segments to a point in which the coil size becomes comparable to the chain backbone. Such a coiling configuration would in fact correspond to the folding dynamics of DNA-linked paramagnetic chains.[45] Therefore, the transition from coiling to folding occurs smoothly, *i.e.* the folding dynamics represent the limit of coiling deformation at very high field strengths. Note that chains undergoing folding dynamics also acquire their clip-like structure in less than a single field cycle.

The field intensities that induce the coiling deformation in the nonlinear regime are not strong enough to sustain synchronous rotation of the end segments within 2/3 of a field period. Instead, the chain ends only deflect slightly in the field's rotational direction. After the initial deflection, the chain ends become arrested as they cannot continue to follow the magnetic field because the driving magnetic torque cannot overcome the viscous drag. Eventually, the magnetic field and the arrested chain ends become orthogonal to each other as the field continues its rotation. Afterward, the magnetic field approaches the arrested ends from the opposite direction as the field approaches the completion of one revolution. This significant misalignment causes the arrested segment to briefly rotate in the opposite direction of rotation. After a cycle, the field reaches the orientation of the deflected ends and resumes their deflection in the direction of rotation. This process creates a rocking deflection in which the segments experience a forward and backward kick within each revolution of the CRMF. Over several cycles, there is a net rotation of the chain ends in the

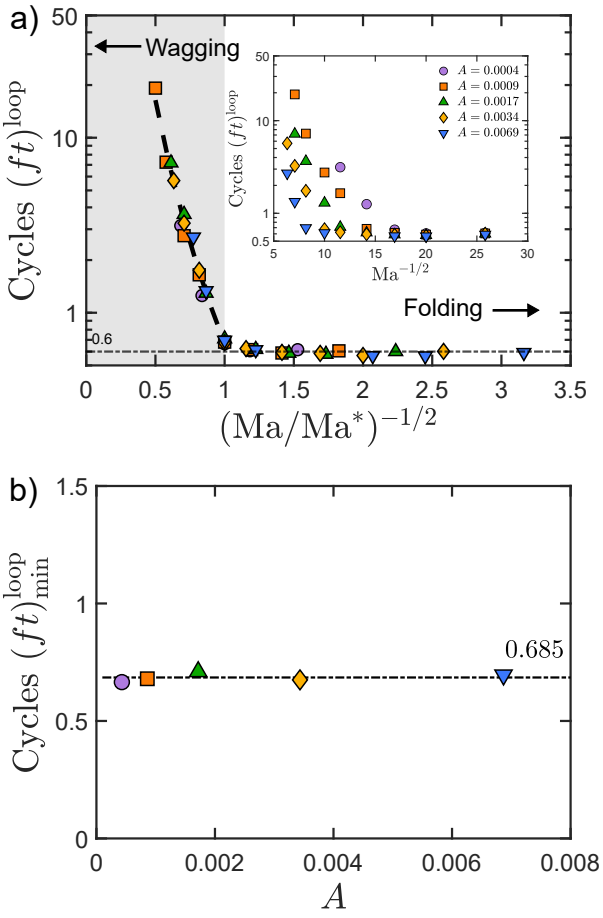

Fig. 5 Time-scale for the formation of the first loop in the coiling dynamics. a) The number of cycles of the external CRMF required to form the first coil, as a function of $\mathrm{Ma}^{-1/2}$ (inset). When normalized by the transition value of Ma^*, it is apparent that for values less than 1, the first coil takes multiple cycles to form, with limiting behavior akin to the wagging dynamics established in[45]. For values greater than 1, all coils form in less than a full cycle, with limiting behavior approaching folding dynamics. The shaded region indicates the nonlinear regime of R_g^{loop} from Fig. 4c, where the number of cycles decreases via a power-law with an exponent of -14/3. (b) Over a range of A , the minimum points of the R_g^{loop} curves all take ≈ 0.685 cycles to coil.

sense of the CRMF. After enough cycles, the deflected portions of the chain develop significant curvature to curl and get in contact with the chain backbone. Ultimately, this leads to the deformation of the ends into circular coiling loops (low δ^{loop}). Increasing field strength (decreasing Ma) for a fixed A signifies an increase in Mn (see Eq. 11), meaning that a stronger field can more readily overcome the bending stiffness of the chain and produce more significant curvature. Therefore, in this nonlinear regime where the magnetic torque cannot overcome the drag, the increasing field strength can produce more pronounced curvature over shorter segments at the chain ends compared to weaker fields, leading to smaller coil sizes that form over fewer cycles of the field rotation. Correspondingly, the coiling shape deviates more and more from the circular morphology as the field strength rises. For a chain with higher A, and thus larger Mn, the lower rigidity for the same field strength allows for the formation of even smaller loops over fewer cycles compared to a stiffer chain, as shown in the inset of Fig. 5a. This is the reason behind the decrease in loop size when comparing the simulations in Fig. 2c and 2e.

A connection can also be built between the nonlinear coiling regime and the wagging dynamics schematized in Fig. 1a. As a decreasing field intensity requires more cycles to form a loop, ultimately a sufficiently weak field will produce a rocking motion that cannot bring the ends in contact with the chain backbone to form a loop within a reasonable time-scale. Therefore, we can conclude that the transition from coiling to the wagging dynamics observed in experimental DNA-linked is also smooth. Essentially, the wagging behavior of these chains represents the limit of coiling deformation at very low field strengths, where the rocking deflection dominates the entire dynamics.

4 Conclusions

We have numerically explored the dynamics of paramagnetic semiflexible filaments as they coil anti-symmetrically in an externally applied CRMF, and demonstrate that the size of the initial coil follows a non-monotonic dependence with $\text{Ma}^{-1/2}$, which can be broken down into a power law decay and a linear increasing regime.

In the power law region, coil sizes are dependent on the value of A, as the field is low enough that the magnetic, elastic, and viscous forces compete to cause a rocking deflection. Thus, the chain ends deflect over multiple rotations of the external field, until forming a first coil with lower asphericity. In the linear region, at higher field strengths, the increase in coil size shows no dependence on A. Here, the greater available magnetic torques and viscous resistance cause the chain ends to deflect synchronously with the external field. This leads to a coil formed in less than a full field rotation with loops of higher asphericity.

Between the power law decay and linearly increasing regime is a transition value. This point can be predicted as a function of A and Ma, and can be interpreted as the change from asynchronous to synchronous dynamics of the chain ends, indicating the transition from a wagging mechanism to a folding mechanism of coiling ends. This transition point also marks the smallest coil size achievable for a chain of a given A.

As such, the morphology and timescales of coils in semiflexible filaments are intricately linked together, but the range of coil shapes and sizes can be achieved by directed manipulation of filament properties and the parameters of the applied CRMF. This, in turn, informs the application, control, and optimization of coiling dynamics in different contextual applications.

Conflicts of interest

There are no conflicts to declare.

Acknowledgements

Acknowledgment is made to the donors of the American Chemical Society Petroleum Research Fund 65274 for partial support and the National Science Foundation under Grant No. 1705703.

Author Contributions

Aldo Spatafora-Salazar: conceptualization, data curation, formal analysis, visualization, writing - original draft, writing - review & editing. Steve Kuei: conceptualization, experiments, writing - original draft, writing - review & editing. Lucas H. P. Cunha: numerical computation, formal analysis, writing - review & editing. Sibani Lisa Biswal: conceptualization, supervision, funding acquisition, writing - review & editing.

Appendix

We perform a torque balance by approximating the deflecting chain ends as a rigid magnetic chain of length ℓ pinned on one of its ends. The deflected end will constitute the entire perimeter of the first loop formed during coiling. Figure 6 illustrates this pinned rigid-rod approximation on a deflected chain segment prior to curling. The moment arm of the force is taken to be the distance from the pinned end. Note that we neglect any bending moments acting on the pinned end because the linear trend of the coil size with field strength being modeled here does not change upon variation of the elastoviscous number (effective chain stiffness).

Assuming a simple dipolar model, the magnetic forces acting on the particles cancel each other because the two nearest neighbors of any given bead exert equal but opposite forces.[43] Since the last bead on the chain only has one neighbor, the magnetic force acting on it is not balanced by other magnetic contributions. Therefore, the magnetic torque on the free end of the chain is computed only from the angular component of the dipolar magnetic force acting on the outermost particle, which has moment arm ℓ from the pinned end. Considering these assumptions, the magnetic torque on the chain is

$$\Gamma_{\text{mag}} = \frac{3\mu_0 m^2 \ell}{4\pi r^4} \sin(2\alpha), \tag{17}$$

where m is the magnitude of the particle magnetization, r is the center-to-center distance between two particles, and α is the angle between the field direction and the orientation of the long-axis of the rigid chain also known as the phase lag angle. For a simple dipolar model, the magnetization is $m = V_p \chi H_0^2 = 4\pi a^3 \chi H_0^2/3$ where V_p is the volume of the spherical particle. The interparticle spacing is set to the separation used in the simulations $r = l_0 = 5a/2$. Substituting m and r into Eq. 17 and simplifying yields the following expression for the magnetic torque

$$\Gamma_{\text{mag}} = \frac{2^6}{3(5)^4} \mu_0 \pi a^2 \chi^2 H_0^2 \ell \sin(2\alpha). \tag{18}$$

In the absence of inertia (due to the low Reynolds number), the magnetic torque is balanced only by an opposing viscous torque mediated by the surrounding fluid. Neglecting hydrodynamic interactions between the beads, the viscous torque on the chain can be expressed as[69]

$$\Gamma_{\text{v}} = \frac{\pi \eta \ell^3}{4} \left(\frac{d\psi}{dt} \right) \tag{19}$$

where ψ is the orientation of the rigid chain and $d\psi/dt$ is its angular velocity. The instantaneous chain angle can be expressed in terms of the phase lag angle and the angle of the CRMF as $\psi = \omega t - \alpha$,[25,43] where $\omega = 2\pi f$ is the angular frequency of the CRMF. Substituting these angles into Eq. 19, the viscous torque becomes

$$\Gamma_{\text{v}} = \frac{\pi \eta \ell^3}{4} \left(\omega - \frac{d\alpha}{dt} \right). \tag{20}$$

Performing a torque balance by equating Equations 18 and 20 yields an expression for the rate of change of the phase lag angle

$$\frac{d\alpha}{dt} = \omega - \frac{2^8 a^2 \mu_0 \chi^2 H_0^2}{3(5)^4 \eta \ell^2} \sin(2\alpha). \tag{21}$$

Assuming that the rigid rod rotates synchronously with the field (which is a valid assumption for the deflecting segments of the chain in the linear size regime based on the time-scale results from Fig. 5a), then the phase lag angle will be at steady state. Therefore, Eq. 21 can be rearranged into the following expression

$$\sin(2\alpha) = \frac{3(5)^4 \eta \omega \ell^2}{2^8 a^2 \mu_0 \chi^2 H_0^2}. \tag{22}$$

The maximum magnetic torque occurs when $\alpha = \pi/4$, for which $\sin(2\alpha) = 1$. Assuming the magnetic torque is a maximum and substituting the Mason number $\text{Ma} = 72\eta\omega/\mu_0\chi^2 H_0^2$ (see Eq. 9) into Eq. 22, we can obtain an expression for the length of the longest rigid chain that can be actuated at a given set of parameters of the CRMF (at a given Ma):

$$\ell = \frac{2^5\sqrt{6}}{5^2} a (\text{Ma})^{-1/2} \tag{23}$$

which states that ℓ depends linearly on the particle radius a and $\text{Ma}^{-1/2}$. Note that Eq. 23 indicates that a rigid chain of length $L \leq \ell$ will rotate synchronously with the magnetic field, but the maximum magnetic torque will be exerted for a length $L = \ell$. If the rigid chain is longer, then the magnetic torque will become time-dependent and will decrease after reaching the maximum torque, making the steady state assumption on the phase lag angle invalid.

In the case of a semiflexible chain, Eq. 23 describes the maximum length of the end segments that can be actuated to rotate synchronously at a given $\text{Ma}^{-1/2}$. Changing $\text{Ma}^{-1/2}$ will correspondingly modify the length of the deflected segment, at least within the linear regime shown in Fig. 4. The entirety of the

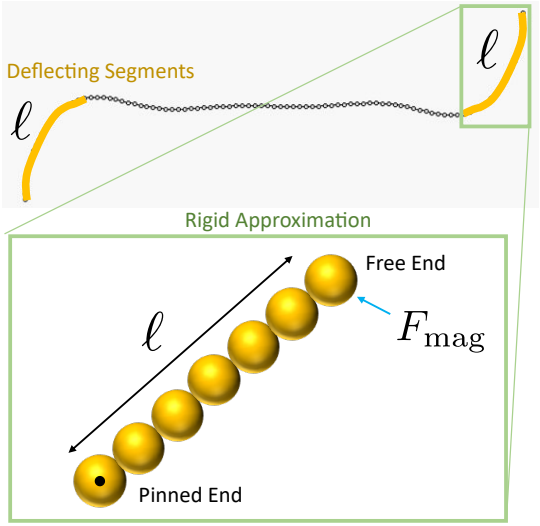

Fig. 6 Approximation of the deflected chain segment of length ℓ as a rigid rod pinned on one end. The magnetic torque is computed from the moment arm ℓ and the angular component of the magnetic force F_{mag} acting on the particle at the free end.

length of a deflected chain segment will eventually wrap around to form the first loop on one side of the chain during the coiling dynamics. Consequently, the length ℓ will constitute the perimeter of the coiled loop. Considering the coiling loops to be ellipses, we can relate their major and minor radii to the perimeter. The exact computation of the perimeter of an ellipse requires an infinite series of terms involving the two principal radii. However, a reasonable approximation for this perimeter can be calculated from $\ell \approx 2\pi(\lambda_1+\lambda_2)^{1/2}/\sqrt{2} \sim 4(\lambda_1+\lambda_2)^{1/2}$, where the λs correspond to the squares of the principal radii of the ellipse best fitting the coiling loop, which is depicted in Fig. 3. Using Eq. 13, we find that $R_g \sim \ell/4$. Substituting this approximation into Eq. 23 yields the following expression for the radius of gyration of the loop in terms of a and $\mathrm{Ma}^{-1/2}$

$$R_g^{\mathrm{loop}} = \frac{2^3\sqrt{6}}{5^2} a(\mathrm{Ma})^{-1/2} \approx 0.7839 a(\mathrm{Ma})^{-1/2}. \tag{24}$$

Normalizing this equation by the total length of the semiflexible chain L and accounting for the normalized particle size used in the simulations of $a/L = 0.004$, Eq. 24 for R_g^{loop} becomes Eq. 16, which we present here once again for completeness:

$$\frac{R_g^{\mathrm{loop}}}{L} \approx 0.00313(\mathrm{Ma})^{-1/2}. \tag{25}$$

This theoretical prediction, arising from the balance of magnetic and viscous torques on a rigid chain pinned on one end, recovers the linear relationship with $\mathrm{Ma}^{-1/2}$ obtained from the simulations. Strikingly, it also predicts essentially the same stiffness-independent slope presented in Fig. 4a.

References

1 O. du Roure, A. Lindner, E. N. Nazockdast and M. J. Shelley, *Annual Review of Fluid Mechanics*, 2019, **51**, 539–572.

2 A. M. Słowicka, H. A. Stone and M. L. Ekiel-Jeżewska, *Physical Review E*, 2020, **101**, 023104.

3 E. Lauga and T. R. Powers, *Reports on Progress in Physics*, 2009, **72**, 096601.

4 H. Manikantan and D. Saintillan, *Physical Review E*, 2015, **92**, 041002.

5 N. Xue, J. K. Nunes and H. A. Stone, *Soft Matter*, 2022, **18**, 514–525.

6 M. Harasim, B. Wunderlich, O. Peleg, M. Kröger and A. R. Bausch, *Physical Review Letters*, 2013, **110**, 108302.

7 Y. Liu, B. Chakrabarti, D. Saintillan, A. Lindner and O. du Roure, *Proceedings of the National Academy of Sciences*, 2018, **115**, 9438–9443.

8 O. L. Forgacs and S. G. Mason, *Journal of Colloid Science*, 1959, **14**, 473–491.

9 S. B. Lindström and T. Uesaka, *Physics of Fluids*, 2007, **19**, 113307.

10 J. LaGrone, R. Cortez, W. Yan and L. Fauci, *Journal of Non-Newtonian Fluid Mechanics*, 2019, **269**, 73–81.

11 P. J. Żuk, A. M. Słowicka, M. L. Ekiel-Jeżewska and H. A. Stone, *Journal of Fluid Mechanics*, 2021, **914**, A31.

12 C. M. Schroeder, *Journal of Rheology*, 2018, **62**, 371–403.

13 S. Yamani, B. Keshavarz, Y. Raj, T. A. Zaki, G. H. McKinley and I. Bischofberger, *Physical Review Letters*, 2021, **127**, 074501.

14 C. A. Browne and S. S. Datta, *Science Advances*, 2021, **7**, eabj2619.

15 S. S. Datta, A. M. Ardekani, P. E. Arratia, A. N. Beris, I. Bischofberger, G. H. McKinley, J. G. Eggers, J. E. López-Aguilar, S. M. Fielding, A. Frishman, M. D. Graham, J. S. Guasto, S. J. Haward, A. Q. Shen, S. Hormozi, A. Morozov, R. J. Poole, V. Shankar, E. S. G. Shaqfeh, H. Stark, V. Steinberg, G. Subramanian and H. A. Stone, *Physical Review Fluids*, 2022, **7**, 080701.

16 L. E. Becker and M. J. Shelley, *Physical Review Letters*, 2001, **87**, 198301.

17 M. Manghi, X. Schlagberger and R. R. Netz, *Physical Review Letters*, 2006, **96**, 068101.

18 B. Qian, T. R. Powers and K. S. Breuer, *Physical Review Letters*, 2008, **100**, 078101.

19 N. Coq, O. du Roure, J. Marthelot, D. Bartolo and M. Fermigier, *Physics of Fluids*, 2008, **20**, 051703.

20 H. R. Vutukuri, B. Bet, R. van Roij, M. Dijkstra and W. T. S. Huck, *Scientific Reports*, 2017, **7**, 16758.

21 J. d. Toonder, F. Bos, D. Broer, L. Filippini, M. Gillies, J. de Goede, T. Mol, M. Reijme, W. Talen, H. Wilderbeek, V. Khatavkar and P. Anderson, *Lab on a Chip*, 2008, **8**, 533.

22 A. Al-Harraq, B. D. Choudhury and B. Bharti, *Langmuir*, 2022, **38**, 3001–3016.

23 E. M. Furst, C. Suzuki, M. Fermigier and A. P. Gast, *Langmuir*, 1998, **14**, 7334–7336.

24 C. Goubault, P. Jop, M. Fermigier, J. Baudry, E. Bertrand and J. Bibette, *Physical Review Letters*, 2003, **91**, 260802.

25 S. L. Biswal and A. P. Gast, *Physical Review E*, 2004, **69**, 041406.

26 H. Singh, P. E. Laibinis and T. A. Hatton, *Langmuir*, 2005, **21**, 11500–11509.

27 B. Yigit, Y. Alapan and M. Sitti, *Soft Matter*, 2020, **16**, 1996–2004.

28 D. Li, S. Banon and S. L. Biswal, *Soft Matter*, 2010, **6**, 4197.

29 T. Yang, D. W. Marr and N. Wu, *Colloids and Surfaces A: Physicochemical and Engineering Aspects*, 2018, **540**, 23–28.

30 R. Mhanna, Y. Gao, I. Van Tol, E. Springer, N. Wu and D. W. M. Marr, *Langmuir*, 2022, **38**, 5730–5737.

31 P. Vázquez-Montejo, J. M. Dempster and M. O. de la Cruz, *Physical Review Materials*, 2017, **1**, 064402.

32 T. Yang, B. Sprinkle, Y. Guo, J. Qian, D. Hua, A. Donev, D. W. M. Marr and N. Wu, *Proceedings of the National Academy of Sciences*, 2020, **117**, 18186–18193.

33 M. Roper, R. Dreyfus, J. Baudry, M. Fermigier, J. Bibette and H. A. Stone, *Journal of Fluid Mechanics*, 2006, **554**, 167.

34 A. Spatafora-Salazar, L. H. P. Cunha and S. L. Biswal, *Journal of Physics: Condensed Matter*, 2022, **34**, 184005.

35 R. Dreyfus, J. Baudry, M. L. Roper, M. Fermigier, H. A. Stone and J. Bibette, *Nature*, 2005, **437**, 862–865.

36 E. M. Gauger, M. T. Downton and H. Stark, *The European Physical Journal E*, 2009, **28**, 231–242.

37 N. Coq, S. Ngo, O. du Roure, M. Fermigier and D. Bartolo, *Physical Review E*, 2010, **82**, 041503.

38 A. Babataheri, M. Roper, M. Fermigier and O. Du Roure, *Journal of Fluid Mechanics*, 2011, **678**, 5–13.

39 F. Martinez-Pedrero, A. Cebers and P. Tierno, *Physical Review Applied*, 2016, **6**, 034002.

40 T. Yang, T. O. Tasci, K. B. Neeves, N. Wu and D. W. M. Marr, *Langmuir*, 2017, **33**, 5932–5937.

41 H. Abdi, R. Soheilian, R. M. Erb and C. E. Maloney, *Physical Review E*, 2018, **97**, 032601.

42 R. Soheilian, H. Abdi, C. E. Maloney and R. M. Erb, *Journal of Colloid and Interface Science*, 2018, **513**, 400–408.

43 I. Petousis, E. Homburg, R. Derks and A. Dietzel, *Lab on a Chip*, 2007, **7**, 1746.

44 A. Vázquez-Quesada, T. Franke and M. Ellero, *Physics of Fluids*, 2017, **29**, 032006.

45 S. Kuei, B. Garza and S. L. Biswal, *Physical Review Fluids*, 2017, **2**, 104102.

46 A. Cebers, *Current Opinion in Colloid & Interface Science*, 2005, **10**, 167–175.

47 A. Cēbers and H. Kalis, *The European Physical Journal E*, 2011, **34**, 30.

48 A. Spatafora-Salazar, D. M. Lobmeyer, L. H. P. Cunha, K. Joshi and S. L. Biswal, *Soft Matter*, 2021, **17**, 1120–1155.

49 N. Casic, S. Schreiber, P. Tierno, W. Zimmermann and T. M. Fischer, *EPL (Europhysics Letters)*, 2010, **90**, 58001.

50 A. C. H. Coughlan, I. Torres-Díaz, J. Zhang and M. A. Bevan, *The Journal of Chemical Physics*, 2019, **150**, 204902.

51 F. Mignolet, A. Darras and G. Lumay, *Physical Review E*, 2022, **106**, 034606.

52 L. H. P. Cunha, J. Zhao, F. C. MacKintosh and S. L. Biswal, *Physical Review Fluids*, 2022, **7**, 034303.

53 J. Rotne and S. Prager, *The Journal of Chemical Physics*, 1969, 8.

54 H. Yamakawa, *The Journal of Chemical Physics*, 1970, 9.

55 E. E. Keaveny and M. R. Maxey, *Journal of Computational Physics*, 2008, **227**, 9554–9571.

56 K. Han, Y. T. Feng and D. R. J. Owen, *International Journal for Numerical Methods in Engineering*, 2010, **84**, 1273–1302.

57 Z. M. Sherman, D. Ghosh and J. W. Swan, *Langmuir*, 2018, **34**, 7117–7134.

58 H. Hertz, *On the contact of rigid elastic solids and on hardness, chapter 6: Assorted papers by H. Hertz*, 1882.

59 S. W. Cranford, L. Han, C. Ortiz and M. J. Buehler, *Soft Matter*, 2017, **13**, 5543–5557.

60 S. Melle, O. G. Calderón, M. A. Rubio and G. G. Fuller, *Physical Review E*, 2003, **68**, 041503.

61 D. Du, E. Hilou and S. L. Biswal, *Physical Review E*, 2016, **93**, 062603.

62 J. Byrom, P. Han, M. Savory and S. L. Biswal, *Langmuir*, 2014, **30**, 9045–9052.

63 J. Zhao, D. Du and S. L. Biswal, *Physical Review E*, 2018, **98**, 012602.

64 H. Arkın and W. Janke, *The Journal of Chemical Physics*, 2013, **138**, 054904.

65 V. Blavatska and W. Janke, *The Journal of Chemical Physics*, 2010, **133**, 184903.

66 S. Melle, O. G. Calderón, M. A. Rubio and G. G. Fuller, *Journal of Non-Newtonian Fluid Mechanics*, 2002, **102**, 135–148.

67 T. G. Kang, M. A. Hulsen, P. D. Anderson, J. M. J. den Toonder and H. E. H. Meijer, *Physical Review E*, 2007, **76**, 066303.

68 Y. Gao, M. A. Hulsen, T. G. Kang and J. M. J. den Toonder, *Physical Review E*, 2012, **86**, 041503.

69 M. Doi and S. F. Edwards, *The Theory of Polymer Dynamics*, Clarendon Press, 1988.